RAA 2019 Vol. **19** No. **10**, 148(8pp) doi: 10.1088/1674–4527/19/10/148

http://www.raa-journal.org *http://iopscience.iop.org/raa*

***R**esearch in*
***A**stronomy and*
***A**strophysics*

Infrared photometric properties of inner and outer parts of HII regions

Anastasiia Topchieva[1], Vitaly Akimkin[1] and Grigorii Smirnov-Pinchukov[2]

[1] Institute of Astronomy, Russian Academy of Sciences, Moscow 119017, Russia; *ATopchieva@inasan.ru*
[2] Max Planck Institute for Astronomy, Königstuhl 17, D-69117 Heidelberg, Germany

Received 2019 March 11; accepted 2019 May 27

Abstract The fact that infrared ring nebulae (IRRNe) are frequently associated with HII regions provides us with an opportunity to study dust at the interface between ionized and neutral gas. In this paper, we analyze the associated infrared (IR) radiation in the range from 8 to 500 μm in the outer and inner parts of 32 IRRNe showing a round shape. We aim to determine the morphology of these objects and possible dust evolution processes based on comparing IR radiation towards the ionized and neutral regions. We calculate six slopes between adjacent wavelengths in their spectral energy distributions to trace the difference in physical conditions inside and outside the ionized regions. Using data on these 32 objects, we demonstrate that their morphology is likely 3D spherical rather than 2D plane-like. The slope between 70 and 160 μm is the most appropriate tracer of dust temperature in the outer envelope. The larger 8-to-24 μm intensity ratio is associated with smaller intensities at mid-IR, indicating that polycyclic aromatic hydrocarbons (PAHs) may indeed be generated due to larger grain destruction. These data are important for the subsequent theoretical modeling, and determining the dust evolution in HII regions and their envelopes.

Key words: stars: massive — ISM: bubbles — dust, extinction — H II regions — infrared: ISM

1 INTRODUCTION

Thanks to infrared (IR) observations by space telescopes *Spitzer*, *WISE*, *Akari* and *Herschel*, more than 8000 HII regions have been discovered (Churchwell et al. 2006, 2007; Anderson et al. 2012, 2014; Bufano et al. 2018), which look like full or open infrared ring nebulae (IRRNe). Most of these objects are identified as HII regions around massive OB stars (Churchwell et al. 2006, 2007) or as Wolf-Rayet stars (Gvaramadze et al. 2010). A specific feature of IRRNe is the presence of an outer ring visible in near-IR, mid-IR and far-IR from 8 to 500 μm, while emission from the inside of the ring is observed only in mid-IR within 24–70 μm, and is significantly suppressed in near- and far-IR. As emission at different wavelengths can be generated mostly by dust grains with a specific size, suppressed 8 μm and far-IR emission from the ionized region can be attributed to a non-uniform distribution of dust particles in the HII regions caused by photo-destruction, radiation pressure or stellar wind (Mathis 1986; Kruegel 2003; Pavlyuchenkov et al. 2013; Mackey et al. 2016; Akimkin et al. 2017).

Statistical analysis of HII regions (see e.g., Anderson et al. 2012; Khramtsova et al. 2013; Anderson et al. 2014; Topchieva et al. 2017b; Mackey et al. 2016) is a powerful tool to advance a further interpretation of observational data and relate them to the results of numerical modeling. This is important because there are still some key questions that lack definite answers. The dominant mechanism for removing dust from HII regions is among them. In Akimkin et al. (2017), we presented a counterintuitive theoretical prediction that the radiative drift of dust is less efficient around stars with higher effective temperatures. Indeed, more energetic stars cause stronger radiation pressure on dust, but they also charge the grains more, which increases the dynamical coupling of dust to the plasma. The combined action of radiation pressure and Coulomb drag force leads to less effective expulsion of dust from stars with higher effective temperatures. Photo-destruction is, in contrast, likely to be more effective in more energetic environments. Thus, one may expect smaller amounts of dust around hotter stars if photo-destruction dominates over radiation pressure in dust removal from the ionized region, and vice versa. The central ionizing stars are not readily identifiable, which hampers the determination of how the

amount of dust in ionized regions depends on stellar effective temperatures. With other things being equal, the dust temperature can potentially serve as an indicator of stellar energetics.

In previous works, we presented a multi-wavelength catalog (Topchieva et al. 2017a, 2018) providing total fluxes for 99 IRRNe at eight wavelengths. Qualitatively, particles with different sizes can be traced through these wavelengths. Emission at 8 μm is mostly generated by tiny polycyclic aromatic hydrocarbons (PAHs), and 24 μm emission comes mostly from very small grains (VSGs) with size ~ 50 Å, whereas larger grains ($< 10^{-5}$ cm) contribute in the 70–500 μm wavelength range.

In this paper, we aim to use dust emission towards the ionized and neutral parts of HII regions to differentiate between their 2D toroidal vs. 3D spherical morphology and to constrain the dust removal mechanisms. To do this, we update our catalog (Topchieva et al. 2018) with new information on radiation fluxes from the inner and outer parts of IRRNe associated with HII regions. In Section 2, we describe the data processing. In Section 3, we analyze spectral differences between the inner and outer parts of IRRNe. In Section 4, we summarize the obtained results.

2 DATA PROCESSING

In this work, we used data from the previously developed catalog (Topchieva et al. 2017a), which includes 99 IRRNe associated with HII regions. The work is based on the 8 μm survey obtained in the GLIMPSE project[1] (Rieke et al. 2004; Fazio et al. 2004), and on the 24 μm MIPSGAL survey[2] (Benjamin et al. 2003; Carey et al. 2009) from the *Spitzer* telescope. We also applied HiGAL[3] data from *Herschel* at wavelengths of 70, 160, 250, 350 and 500 μm. Point sources were removed from the images using an automatic cleaning procedure described in Topchieva et al. (2017a). The search and removal of point sources were carried out in three subsequent stages depending on the brightness of the stars. In our previous study, we fitted 99 IRRNe with ellipses to determine the position of the center for each nebula, its size, the degree of asymmetry and the position angle. Based on these results, we selected 32 objects, for which the eccentricity of the fitted ellipses does not exceed 0.6 at the wavelength of 8 μm, and the semi-major axis exceeds $20''$. These 'perfect' IRRNe are further analyzed in this study. The size and position of the center of the aperture superimposed on the source are also determined from the 8 μm images, as well as the values of the major (a) and minor (b) axes (Topchieva et al. 2017a). We used 8 μm data to find the size of the object as the radiation from the outer ring at 8 μm is present for all objects in the sample and the boundaries of the object can be defined clearly.

For the selected 32 objects, we define fluxes at seven wavelengths ranging from 8 to 500 μm for both the ejected envelope and for the inner ionized zone. To define the apertures for the flux derivation in a standardized way, we employed the following procedure. As the typical full width of the outer rings in near-IR is $20\% - 50\%$ of its radius, we define the inner aperture as an ellipse with major and minor axes $a_{\rm inn} = 0.7a$ and $b_{\rm inn} = 0.7b$ respectively. This choice allows us to exclude most radiation from the envelope side, but surely not the radiation coming from the possible front and back walls in case of 3D morphology. The outer aperture lies between the inner aperture and encompassing ellipse with $a_{\rm out} = 1.3a$ and $b_{\rm out} = 1.3b$. An example of such choice of apertures for N80 is presented in Figure 1. We intentionally do not subtract the 'background' radiation because its estimate using the radiation far from the object in the image plane may introduce wavelength dependent bias, which is detrimental for the purposes of this study. This is caused by small but noticeable differences in the radiation spectrum of matter surrounding the object from different sides.

3 COMPARISON OF SPECTRAL CHARACTERISTICS OF INNER AND OUTER REGIONS

3.1 Spectral Energy Distributions

For all wavelengths (8, 24, 70, 160, 250, 350 and 500 μm) we used the same aperture, which is determined for each object individually, as described above. The fluxes from the inner and outer parts of the objects are presented in Tables 1 and 2, as well as the solid angles of the apertures. By dividing the fluxes by corresponding solid angles, one can procure the average intensities within inner and outer regions. This allows us to generate the spectral energy distribution (SED) in a unified way for all 32 objects. The SEDs for inner and outer regions are presented in Figure 2. The characteristic feature of these SEDs is the presence of two components, thermal emission from cold and large dust grains peaking at $\sim$ 100 μm and near-IR stochastically generated emission from PAHs and VSGs.

[1] Galactic Legacy Infrared Mid-Plane Survey Extraordinaire

[2] 24 and 70 Micron Survey of the Inner Galactic Disk with MIPS

[3] `https://tools.asdc.asi.it/HiGAL.jsp`

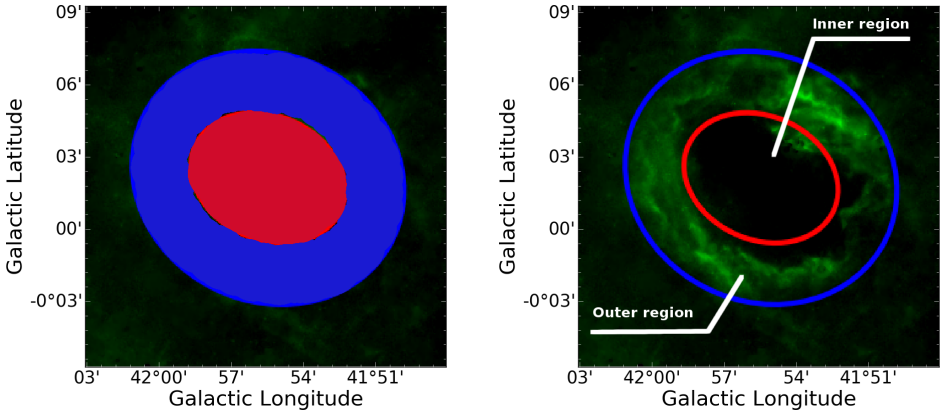

Fig. 1 An example of apertures for calculating the flux from the outer and inner regions for N80. The *green* areas in the *right* panel represent 8 μm emission.

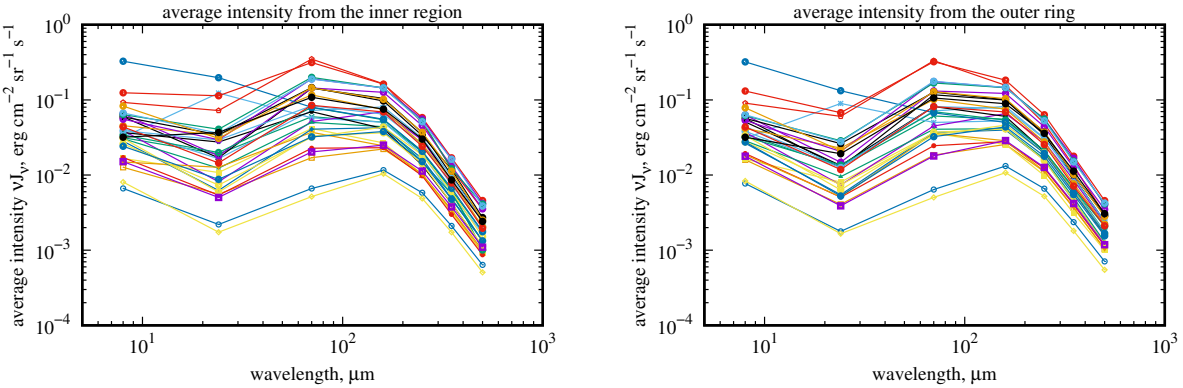

Fig. 2 SEDs from inner (*left*) and outer (*right*) parts of 32 IRRNe.

3.2 Spectral Indices

To numerically characterize the SED, we utilize the commonly employed spectral index, which can be defined as

$$\alpha = \frac{d \log I_\nu}{d \log \nu} \,. \qquad (1)$$

In practice, we define the spectral index for two adjacent frequencies ν_1 and ν_2 as $\alpha_{12} = \log(I_1/I_2)/\log(\nu_1/\nu_2)$. A comparison of the spectral indices in the inner and outer regions is depicted in Figure 3.

The spectral indices are calculated only for neighboring wavelengths as they are the most informative for our study. The associated uncertainty is calculated under the assumption of a fixed 15% uncertainty in the flux. The diagonal line on the graph delineates the position of equal indices in the inner and outer regions. One can ascertain that the spectral indices calculated between 160 and 250 μm, 250 and 350 μm, and 350 and 500 μm ($\alpha_{160/250}, \alpha_{250/350}, \alpha_{350/500}$ respectively) are very similar in the direction of the ionized region and of the neutral ejected envelope. This can be attributed to two reasons. First, the spatial resolution at these wavelengths may not be good enough to resolve the structure of the HII regions. Second, the emission at these wavelengths is likely to be dominated by the surrounding envelope, and, in the case

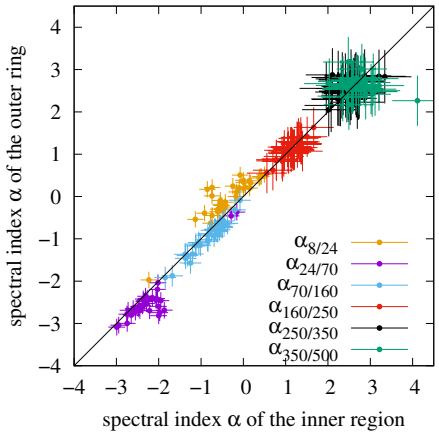

Fig. 3 The relationship between spectral indices in the inner and outer regions for the 32 IRRNe. The *diagonal line* represents equal spectral indices in the inner and outer parts of HII regions. Note the difference between spectral indices $\alpha_{8/24}, \alpha_{24/70}, \alpha_{70/160}$ in the inner and outer parts.

Table 1 Fluxes and Solid Angles for the Inner Regions of 32 IRRNe

Object	$(l^\circ_{\rm gal}; b^\circ_{\rm gal})$	F_8 (Jy)	F_{24} (Jy)	F_{70} (Jy)	F_{160} (Jy)	F_{250} (Jy)	F_{350} (Jy)	F_{500} (Jy)	Ω (10^{-8} sr)
S123[2]	(312.97; –0.43)	43.1	46.8	502.4	1354.0	840.2	372.2	148.1	164
S167[2]	(301.62; –0.34)	90.5	89.9	790.4	3173.0	2476.0	1255.0	543.2	1250
CN111[2]	(8.31; –0.08)	34.8	41.4	531.0	1351.0	812.1	348.5	132.1	76.9
N67[2]	(35.54; 0.01)	6.8	12.3	113.3	218.9	136.9	59.5	23.8	19.9
N90[2]	(43.77; 0.06)	11.9	15.6	140.5	417.8	295.3	136.4	54.9	86.5
N96[2]	(46.94; 0.37)	0.9	1.8	20.3	29.8	17.7	7.7	3.1	5.12
N98[2]	(47.02; 0.21)	13.1	12.4	152.6	353.5	233.8	100.1	41.5	70.3
N102[2]	(49.69; –0.16)	19.6	49.8	425.3	644.2	418.3	197.5	82.0	121
N121[2]	(55.44; 0.88)	0.9	0.6	5.2	24.0	17.6	8.7	3.6	10.6
N4[2]	(11.89; 0.74)	51.4	115.4	852.3	1161.0	592.2	257.6	95.9	128
N20[2]	(17.91; –0.68)	10.3	8.7	110.8	346.2	230.3	105.2	37.6	36.6
N14[2]	(14.00; –0.13)	66.8	182.7	1475.0	1741.0	973.4	398.0	153.3	49.1
N23[2]	(18.67; –0.23)	3.6	6.1	76.6	116.1	62.8	30.9	10.2	5.51
N32[2]	(23.90; 0.07)	3.2	5.1	96.5	166.8	100.6	41.0	15.1	5.30
N33[2]	(24.21; –0.04)	3.4	6.5	93.6	155.1	87.7	28.4	13.8	4.93
N28[2]	(21.35; –0.13)	6.5	7.2	99.5	160.5	91.1	38.7	12.3	7.24
N51[2]	(29.15; –0.25)	42.1	24.3	395.6	998.0	604.9	251.5	97.3	125
N60[2]	(33.81; –0.14)	5.1	5.0	86.4	161.1	87.9	40.0	14.2	10.7
N70[2]	(37.75; –0.11)	3.1	10.8	93.1	148.0	92.2	36.9	14.8	9.02
N80[2]	(41.93; 0.03)	14.6	14.5	171.8	483.0	340.8	159.3	66.0	36.2
G027.492+0.192[3]	(27.49; 0.19)	6.9	16.0	226.2	241.6	115.1	39.1	16.1	6.78
MWP1G032731+002120[1]	(32.72; 0.21)	3.0	35.0	47.8	95.4	55.9	22.7	10.0	8.70
MWP1G030250+002413[1]	(30.24; 0.24)	6.7	5.7	142.0	237.4	129.5	49.3	17.9	10.4
MWP1G017626+000493[1]	(17.62; 0.04)	2.1	1.3	24.6	76.2	49.7	19.7	8.5	5.03
MWP1G018580+003400S[1]	(18.58; 0.34)	1.6	1.8	22.3	44.9	24.0	12.4	4.1	1.91
MWP1G048422+001173[1]	(48.42; 0.11)	2.8	1.8	35.9	85.9	51.9	21.4	8.4	9.25
MWP1G024558–001329[1]	(24.55; –0.13)	13.5	11.1	261.1	522.4	294.4	119.1	45.9	19.0
MWP1G037196–004296[1]	(37.19; –0.42)	1.9	3.4	39.6	62.1	36.7	15.5	3.5	5.24
MWP1G032057+000783[1]	(32.05; 0.07)	7.6	17.2	142.9	253.0	157.3	63.5	25.2	18.0
MWP1G018743+002521[1]	(18.74; 0.25)	3.4	7.6	76.4	111.3	60.2	28.3	9.5	6.89
MWP1G037349+006876[1]	(37.35; 0.68)	44.5	80.6	95.1	150.5	87.9	39.7	15.0	12.5
MWP1G024731+001580[1]	(24.73; 0.15)	4.6	7.3	113.3	198.3	109.5	48.6	16.5	6.3

[1] Simpson et al. (2012); [2] Churchwell et al. (2006); [3] Egan et al. (2003).

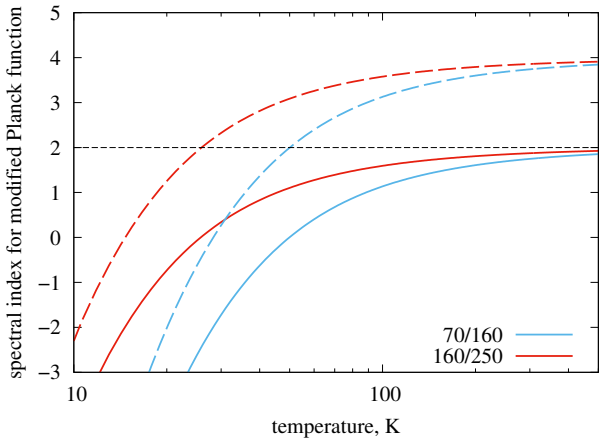

Fig. 4 The spectral index α between 70 and 160 μm (*blue*) and 160 and 250 μm (*red*) for the modified blackbody emission. *Solid* and *dashed lines* demarcate optically thick and optically thin limits, respectively.

of 3D spherical morphology, the inner aperture mostly receives emission from the front and back sides of the object, but not from the ionized vicinity of the central star(s).

The spectral indices $\alpha_{8/24}, \alpha_{24/70}, \alpha_{70/160}$ are clearly different in the inner and outer parts. If the points in Figure 3 lie above the diagonal line, then this means that the ratio of the shorter-wavelength intensity to longer-wavelength intensity is higher in the outer region. This case is represented by the slope between 8 and 24 μm, $\alpha_{8/24}$, and is a simple consequence of the ring-like morphology at 8 μm, while intensities at 24 μm are comparable in the inner and outer regions. This leads to a smaller difference between intensities at 8 and 24 μm in the outer region than in the inner region. As the 8 μm emission is dominated by PAHs and 24 μm emission comes mostly from the VSGs, the slope $\alpha_{8/24}$ is probably uninformative regarding the thermal structure, but rather reflects the density distribution of PAHs and VSGs.

The spectral indices $\alpha_{24/70}, \alpha_{70/160}$ are definitely larger within the inner aperture than in the outer aperture (check magenta and blue dots in Fig. 3). This is exactly what is expected for an object which is hotter inside and colder outside. The 24 μm emission is stochastically generated, which makes it harder to use as a tracer of temperature. Meanwhile, the emission at $70 - 160$ μm is likely *not*

Table 2 Fluxes and Solid Angles for the Outer Rings of 32 IRRNe

Object	$(l^\circ_{\rm gal}; b^\circ_{\rm gal})$	F_8 (Jy)	F_{24} (Jy)	F_{70} (Jy)	F_{160} (Jy)	F_{250} (Jy)	F_{350} (Jy)	F_{500} (Jy)	Ω (10^{-8}sr)
S123[2]	(312.97; –0.43)	120.4	69.0	1243.0	3824.0	2432.0	1051.0	424.2	66.8
S167[2]	(301.62; –0.34)	257.3	178.2	1869.0	8795.0	6872.0	3445.0	1478.0	511
CN111[2]	(8.31; –0.08)	90.5	80.4	1278.0	3359.0	1995.0	826.8	311.2	31.4
N67[2]	(35.54; 0.01)	18.6	20.6	283.5	586.0	347.8	155.5	58.1	8.12
N90[2]	(43.77; 0.06)	36.8	28.1	372.3	1181.0	800.5	370.2	148.1	35.3
N96[2]	(46.94; 0.37)	2.2	3.3	43.1	69.6	42.03	18.4	8.5	2.09
N98[2]	(47.02; 0.21)	36.3	28.5	403.3	1046.0	722.2	331.0	133.6	28.7
N102[2]	(49.69; –0.16)	60.3	49.8	1015.0	1847.0	1134.0	522.0	209.2	49.2
N121[2]	(55.44; 0.88)	2.4	1.4	12.4	60.8	46.0	22.3	9.6	4.38
N4[2]	(11.89; 0.74)	173.7	137.5	2440.0	4125.0	2196.0	914.2	344.0	52.4
N20[2]	(17.91; –0.68)	27.1	21.7	291.2	901.8	606.2	264.0	100.9	14.9
N14[2]	(14.00; –0.13)	172.1	265.3	3693.0	4792.0	2593.0	1019.0	374.0	20.1
N23[2]	(18.67; –0.23)	8.4	11.5	163.2	295.9	170.5	64.8	26.5	2.25
N32[2]	(23.90; 0.07)	7.5	8.7	216.7	412.5	244.6	103.4	35.3	2.17
N33[2]	(24.21; –0.04)	8.1	11.3	193.0	382.6	228.4	88.1	34.0	2.01
N28[2]	(21.35; –0.13)	15.2	12.1	217.3	401.2	225.0	86.3	33.9	2.95
N51[2]	(29.15; –0.25)	112.1	63.4	1082.0	2738.0	1629.0	668.5	251.5	51.2
N60[2]	(33.81; –0.14)	12.5	10.1	203.4	394.0	226.6	88.9	37.5	4.37
N70[2]	(37.75; –0.11)	7.7	13.8	223.3	427.8	269.8	118.6	46.0	3.68
N80[2]	(41.93; 0.03)	41.9	27.5	370.9	1358.0	932.9	431.1	174.5	88.5
G027.492+0.192[3]	(27.49; 0.19)	16.3	32.7	526.1	565.9	273.2	105.0	33.7	2.77
MWP1G032731+002120[1]	(32.72; 0.21)	7.1	62.4	101.9	244.1	149.8	64.5	25.3	3.55
MWP1G030250+002413[1]	(30.24; 0.24)	15.7	10.4	284.1	552.6	296.0	113.5	41.9	4.25
MWP1G017626+000493[1]	(17.62; 0.04)	4.9	2.9	52.7	176.3	115.5	50.2	19.0	2.05
MWP1G018580+003400S[1]	(18.58; 0.34)	3.5	3.5	44.3	103.1	63.9	27.0	10.0	4.67
MWP1G048422+001173[1]	(48.42; 0.11)	6.5	4.0	79.6	195.7	122.7	48.8	19.1	3.78
MWP1G024558–001329[1]	(24.55; –0.13)	31.9	22.4	582.4	1237.0	695.8	278.8	110.3	7.76
MWP1G037196–004296[1]	(37.19; –0.42)	4.5	5.6	85.0	150.9	92.3	40.7	18.1	2.14
MWP1G032057+000783[1]	(32.05; 0.07)	18.4	18.1	341.8	739.4	457.8	216.2	86.0	7.34
MWP1G018743+002521[1]	(18.74; 0.25)	7.6	12.5	162.7	276.9	158.3	61.4	25.3	2.81
MWP1G037349+006876[1]	(37.35; 0.68)	106.9	132.5	196.6	334.8	203.2	86.1	34.8	5.10
MWP1G024731+001580[1]	(24.73; 0.15)	10.6	14.0	260.1	493.4	277.5	109.8	44.4	2.57

[1] Simpson et al. (2012); [2] Churchwell et al. (2006); [3] Egan et al. (2003).

stochastic and comes from the dust with relatively similar size distribution in the inner and outer regions (Akimkin et al. 2017). This makes the color $\alpha_{70/160}$ the best proxy of dust temperature in HII regions.

For illustrating the spectral index dependence on the dust temperature, we calculate it for the case of modified blackbody emission $I_\nu = (1 - e^{-\tau_\nu})B_\nu(T)$. Here $B_\nu(T)$ is the Planck function for a given dust temperature and τ_ν is the optical depth. The corresponding spectral index is

$$\alpha = 3 - \frac{x}{1 - e^{-x}} + \frac{\tau_\nu}{e^{\tau_\nu} - 1}\beta, \qquad (2)$$

where $x = h\nu/(k_B T)$ and $\beta = d\log \varkappa_\nu / d\log \nu$ is the opacity index characterizing the spectral properties of the dust opacity coefficient $\varkappa_\nu$, cm^2 g^{-1}. To compute $\varkappa_\nu$ we use the same absorption efficiency factors for silicate and carbonaceous grains as in Akimkin et al. (2017), but assume another grain size distribution. In this paper we adopt a power-law size distribution with slope -3.5, grain sizes between 0.005 and 0.25 μm and mass ratio 0.2:0.8 between carbonaceous and silicate dust. The corresponding spectral indices $\alpha_{70/160}$ and $\alpha_{160/250}$ for the cases of optically thin and thick emission are presented in Fig. 4.

The horizontal dashed line signifies the Rayleigh-Jeans limit $\alpha = 2$ in optically thick media (the corresponding limit in the optically thin case is $\alpha = 2 + \beta$). Note that α monotonically increases with temperature. The observed values of $\alpha_{70/160}$ lie between -2 and 0, which correspond to a temperature range of $20 - 30$ K. While the inner values of $\alpha_{70/160}$ are definitely larger than the outer ones, indicating hotter interiors, the difference between them is quite small and translates to a corresponding difference in temperatures smaller than several kelvins. One may expect a much larger difference considering the temperature gradient between the ionized region and neutral envelope. This is again indicative of 3D morphology and a corresponding significant contribution from the envelope to the radiation in the inner aperture. To restore the dust properties inside HII regions, a more detailed approach is needed.

3.3 Signs of Dust Evolution Processes

One of our aims is to make a step towards disentangling the possible mechanisms for removing dust from the HII regions. Photo-destruction is more efficient around more

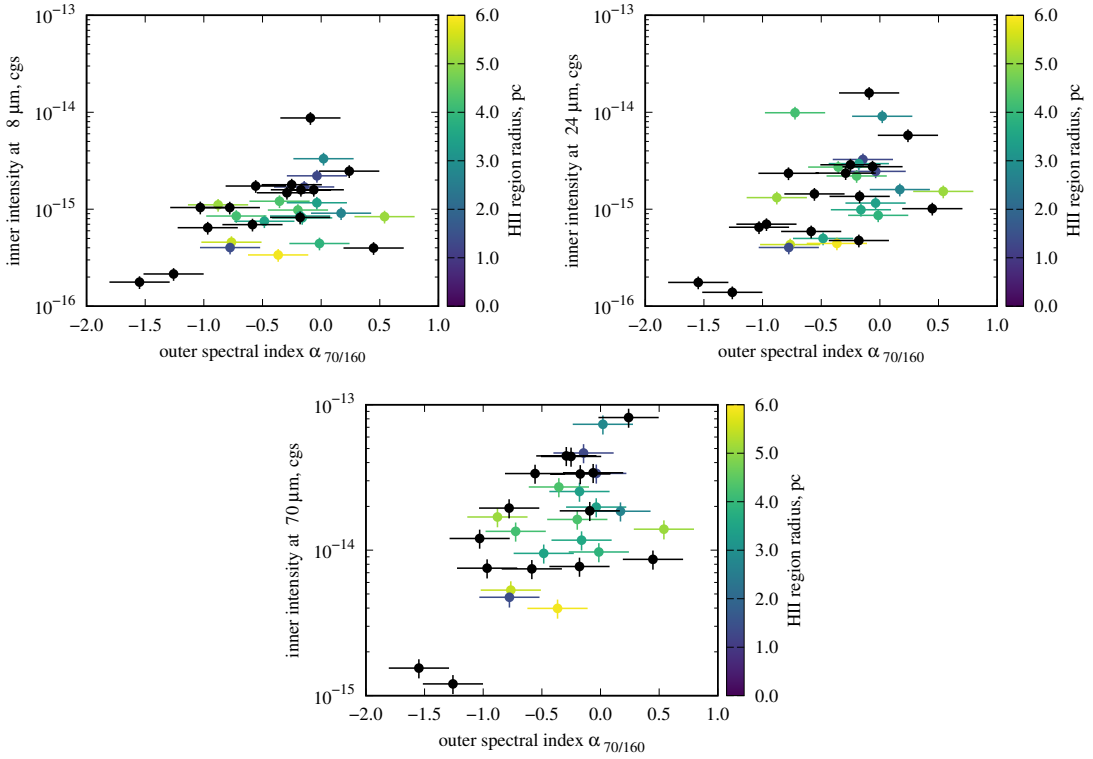

Fig. 5 Average inner intensity at 8, 24 and 70 µm as a function of the spectral index $\alpha_{70/160}$ in the outer region. *Dot color* signifies the linear size of the ionized region (*black* if not known).

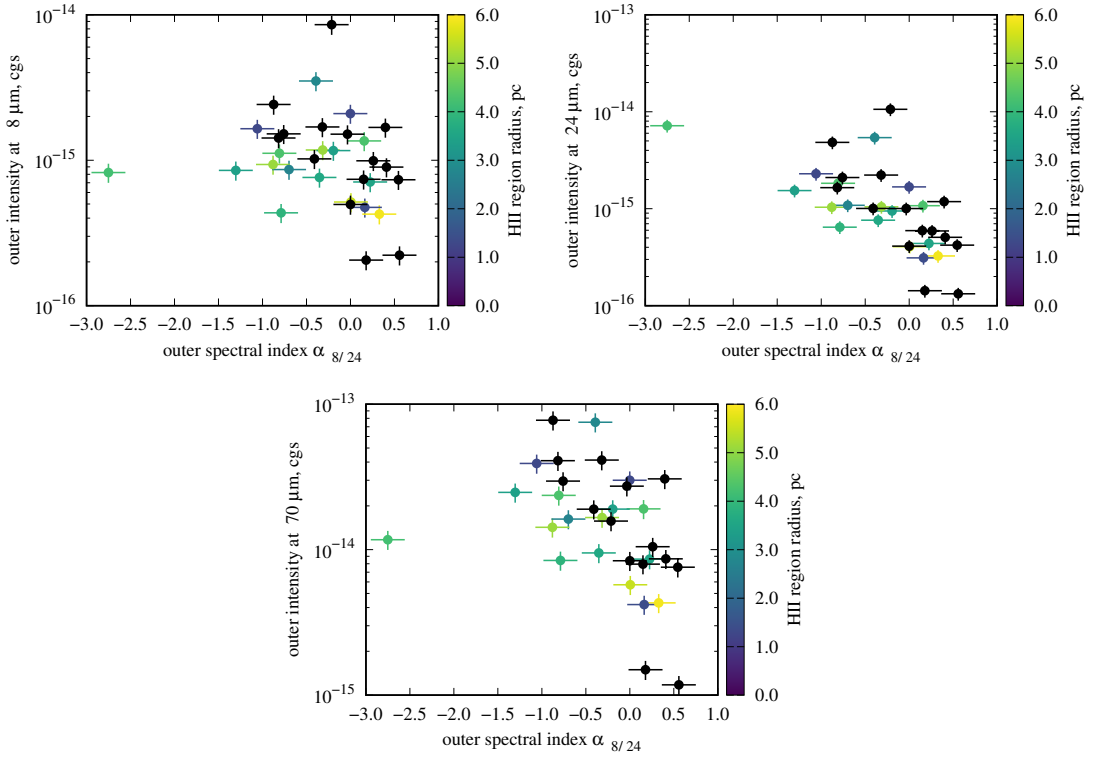

Fig. 6 Average outer intensity at 8, 24 and 70 µm as a function of the spectral index $\alpha_{8/24}$. *Dot color* signifies the linear size of the ionized region (*black* if not known).

energetic stars, but dust removal via radiative drift is more efficient around less energetic stars. The balance between radiation pressure and friction of charged dust with plasma favors the latter around stars with higher effective temperatures (Akimkin et al. 2017). Thus, in the pure drift (no destruction) model, one may expect more dust around more energetic stars. On top of that, both mechanisms should operate with different efficiencies for different grain sizes as photo-destruction is necessary to explain the ring emission at 8 μm (Pavlyuchenkov et al. 2013).

Because the color index $\alpha_{70/160}$ positively correlates with dust temperature and is not very sensitive to the amount of dust in the optically thin regime, it can be regarded as an indicator of the envelope temperature. The envelope temperature depends on the distance to the ionizing star and stellar effective temperature. The former can be accounted for if the distance to the source is known, which is true for 17 of 32 our sources. Thus one may consider $\alpha_{70/160}$ as a rough proxy of the stellar effective temperature. The average intensity inside the inner aperture depends on both temperature and amount of matter in the direction to the central ionizing source. The critical question here is the proportion between surface densities of dust in the envelope and in the HII region itself. In the case of 3D morphology of IR bubbles, the amount of dust in the neutral envelope is likely sufficiently higher than in the inner ionized region, while 2D toroidal morphology implies that dust, which emits radiation within the inner aperture, is actually located inside the ionized region. In Figure 5, we plot the dependence of average intensity within the inner aperture at 8, 24 and 70 μm on the outer spectral index $\alpha_{70/160}$.

In the case of 2D ring morphology (no contribution of the envelope to the inner aperture) and strong photo-destruction of PAHs and other grains emitting at $8-70$ μm, one may expect an anti-correlation between the presented parameters. Obviously, this is not what is observed, leaving us with several options. First, the increase in the inner intensity with $\alpha_{70/160}$ can be simply explained by the higher temperature envelope contributing to the intensity towards the ionized region. Second, the observed behavior may imply a better retention of dust around more energetic stars. Third, moderate photo-destruction may be veiled by the stronger emission of grains surviving the destruction.

The other interesting relation is the map $\alpha_{8/24}$ vs. intensity at 8, 24 and 70 μm in the outer regions (Fig. 6). The variation of $\alpha_{8/24}$ can be primarily caused by variations in intensity at 8 μm, 24 μm or both. Theoretically, if larger values of $\alpha_{8/24}$ were determined solely by the increase in 8 μm intensity with relatively constant 24 μm intensity, then there would be a positive correlation between $\alpha_{8/24}$ and intensity at 8 μm. In the second case (constant 8 μm, varying 24 μm), the anti-correlation between $\alpha_{8/24}$ and intensity at 24 μm would be expected. In the third case (both intensities are varying), no clear trends should be present. As can be ascertained from the first and second panels of Figure 6, the second case is more likely, i.e., the variations of $\alpha_{8/24}$ are caused mostly by the variation in 24 μm emission. The slope $\alpha_{8/24}$ can trace the relative abundance between PAHs and VSGs (with larger values of $\alpha_{8/24}$ corresponding to the larger PAH fraction). The intensity at 70 μm depends on both the surface density of dust and its temperature. Thus, the distribution as seen in the third panel of Figure 6 may be interpreted as observational evidence of the transformation of large dust into PAHs. We plan to investigate the validity of this hypothesis using theoretical modeling with the tools MARION and SHIVA (Akimkin et al. 2017; Murga et al. 2016) in future studies.

4 CONCLUSIONS

We present an extension of the IRRN catalog by Topchieva et al. (2017b) based on *Spitzer* and *Herschel* data. We selected 32 of 99 objects with the most regular rounded shapes and calculated fluxes separately from their inner parts and outer rings at seven wavelengths from 8 to 500 μm. The outer rings correspond to the neutral ejected envelopes, while inner apertures may catch both the radiation from ionized parts of the objects and from the front and back walls of the neutral envelopes. From analysis of the spectral slopes in the inner and outer SEDs of the whole ensemble, we found that:

- The spectral index $\alpha_{70/160}$ between 70 and 160 μm is the most appropriate tracer of dust temperature in the envelope. The use of shorter wavelengths is complicated by the stochastic nature of emission by PAHs and VSGs, while the longer wavelengths suffer from insufficient spatial resolution hampering the differentiation between inner and outer parts of HII regions. More importantly, the emission from dust heated to the envelope temperatures ($20-30$ K) lies between 70 and 160 μm, which ensures good sensitivity of $\alpha_{70/160}$ to the dust temperature;
- The difference between the spectral indices $\alpha_{24/70}$ and $\alpha_{70/160}$ of the inner and outer regions does indicate hotter interiors, but is too small in view of expected temperature difference of ionized and neutral parts of the regions. This indicates that the inner aperture is significantly contaminated by the envelope radiation,

i.e., hints at 3D rather than 2D morphology for IR bubbles.

– Objects with hotter envelopes (traced by larger $\alpha_{70/160}$) are more likely to show higher radiation intensity from the inner parts at 8, 24 and 70 μm. Again, this is a signature of a heated spherical envelope (hotter dust produces more radiation) and unfortunately does not allow us to differentiate between radiation pressure and photo-destruction as the dominant mechanism removing dust from ionized regions. (More energetic stars favor better photo-destruction and less effective radiation drift). However, a 2D ring-like morphology with dominating photo-destruction can be excluded based on these observations.
– The prevalence of PAHs over VSGs (if traced by $\alpha_{8/24}$) is accompanied by smaller fluxes at 24 and 70 μm. This may provide an observational indication that PAHs are formed due to the destruction of larger grains.

Proper modeling tackling dust destruction and dynamics in expanding HII regions is needed to support these conclusions from a theoretical point of view (Murga et al. 2016; Akimkin et al. 2017). This could allow us to determine how different dust evolution processes (photo-destruction, radiative drift, aromatization) manifest themselves in the IR images.

Acknowledgements The authors are grateful to Ya. N. Pavlyuchenkov, D. S. Wiebe and M. S. Kirsanova for useful comments. We also thank the referee for a thorough and careful reading of the manuscript. The work was supported by a grant from the Russian Foundation for Basic Research (18–32–00384). We also thank the developers of the NumPy (Oliphant 2006), SciPy (Jones et al. 2001) and Matplotlib (Hunter 2007) Python packages.

References

Akimkin, V. V., Kirsanova, M. S., Pavlyuchenkov, Y. N., & Wiebe, D. S. 2017, MNRAS, 469, 630
Anderson, L. D., Bania, T. M., Balser, D. S., et al. 2014, ApJS, 212, 1
Anderson, L. D., Zavagno, A., Barlow, M. J., et al. 2012, A&A, 537, A1
Benjamin, R. A., Churchwell, E., Babler, B. L., et al. 2003, PASP, 115, 953
Bufano, F., Leto, P., Carey, D., et al. 2018, MNRAS, 473, 3671
Carey, S. J., Noriega-Crespo, A., Mizuno, D. R., et al. 2009, PASP, 121, 76
Churchwell, E., Povich, M. S., Allen, D., et al. 2006, ApJ, 649, 759
Churchwell, E., Watson, D. F., Povich, M. S., et al. 2007, ApJ, 670, 428
Egan, M. P., Price, S. D., Kraemer, K. E., et al. 2003, VizieR Online Data Catalog, 5114
Fazio, G. G., Hora, J. L., Allen, L. E., et al. 2004, ApJS, 154, 10
Gvaramadze, V. V., Kniazev, A. Y., Hamann, W.-R., et al. 2010, MNRAS, 403, 760
Hunter, J. D. 2007, Computing in Science and Engineering, 9, 90
Jones, E., Oliphant, T., Peterson, P., et al. 2001, SciPy: Open Source Scientific Tools for Python
Khramtsova, M. S., Wiebe, D. S., Boley, P. A., & Pavlyuchenkov, Y. N. 2013, MNRAS, 431, 2006
Kruegel, E. 2003, The Physics of Interstellar Dust (Bristol, UK: The Institute of Physics)
Mackey, J., Haworth, T. J., Gvaramadze, V. V., et al. 2016, Astronomy and Astrophysics, 586, A114
Mathis, J. S. 1986, PASP, 98, 995
Murga, M. S., Khoperskov, S. A., & Wiebe, D. S. 2016, Astronomy Reports, 60, 669
Oliphant, T. 2006, NumPy: A Guide to NumPy (USA: Trelgol Publishing)
Pavlyuchenkov, Y. N., Kirsanova, M. S., & Wiebe, D. S. 2013, Astronomy Reports, 57, 573
Rieke, G. H., Young, E. T., Engelbracht, C. W., et al. 2004, ApJS, 154, 25
Simpson, R. J., Povich, M. S., Kendrew, S., et al. 2012, MNRAS, 424, 2442
Topchieva, A. P., Wiebe, D. S., Kirsanova, M. S., & Krushinskii, V. V. 2017a, Astronomy Reports, 61, 1015
Topchieva, A., Wiebe, D., Kirsanova, M., & Krushinsky, V. 2017b, in Astronomical Society of the Pacific Conference Series, 510, Stars: From Collapse to Collapse, eds. Y. Y. Balega, D. O. Kudryavtsev, I. I. Romanyuk, & I. A. Yakunin, 98
Topchieva, A., Wiebe, D., & Kirsanova, M. S. 2018, RAA (Research in Astronomy and Astrophysics), 18, 091